



TECHNICAL ARTICLE

# Research on the Large Plastic Deformation Damage and Shock Resistance of 7055 Aluminum Alloy

PING ZHANG,<sup>1,2</sup> YOUQIANG WANG,<sup>1</sup> HENG LUO,<sup>1</sup> SHENWEN LONG,<sup>1</sup>  
and CONG WEI<sup>1</sup>

1.—School of Mechanical Engineering, Qingdao University of Technology, Qingdao 266520, Shandong, China. 2.—e-mail: 18661660729@163.com

We used the split Hopkinson dynamic impact test and ABAQUS finite element simulation to study the damage mechanism of dynamic impacts on the 7055-T4 aluminum alloy. The results show that the energy absorption phenomenon occurs when the dynamic impact temperature is 220°C. There is a clear positive correlation between the size of the precipitated phase and the dynamic impact temperature. The regression effect of the 7055-T4 aluminum alloy is most obvious when the dynamic impact temperature is 320°C. The adiabatic temperature rise model in the dynamic impact shear zone and the damage model considering the adiabatic temperature increase are established. Moreover, the above model has high accuracy and is verified by projectile impact simulation.

## INTRODUCTION

The 7055 aluminum alloy is a commonly used lightweight material in aeronautical manufacturing, popular for its low density, high specific strength and specific rigidity. Yang et al.<sup>1</sup> investigated ultrasonic impact treatment on the surface of the 6082 aluminum alloy MIG welded joint. Their results show that as adapting the impact current and impact time were 1.0A/2 min, 1.0A/5 min, 1.5A/2 min and 1.5A/5 min, the thicknesses of the surface plastic deformation layer were 35  $\mu\text{m}$ , 45  $\mu\text{m}$ , 40  $\mu\text{m}$  and 60  $\mu\text{m}$ , respectively. Yang et al.<sup>2</sup> studied dynamic mechanical properties and constitutive equations of a 7N01 aluminum alloy. Their results indicate that the 7N01 Al alloy exhibits a certain susceptibility to strain-rate dependence and a significant temperature susceptibility. The flow stress increases with the decrease of deforming temperature or the increase in strain rate. The Johnson–Cook constitutive equation for the 7N01 Al alloy was obtained by fitting the quasistatic tests data and Hopkinson bar experimental data using the methods of variable separation and nonlinear fitting. The fitting curve is consistent with the curve obtained by experimental results. Tajally et al.<sup>3</sup> analyzed the behavior of deformation fractures in the 6061 aluminum alloy under impact. The results

show that there was no obvious change in fracture behavior under both impact loading and sub-static tensile. The deformation band at the specimen surface is different with different pendulum heights. When the pendulum height reaches 141°, “white deformation bands” appear. Considering that the usual service environment of the 7055 aluminum alloy is 8000 m above sea level, the flow characteristics of the boundary layer and the dynamic impact of airflow have great influence on its performance. In this article, the mechanism of microstructural evolution during the dynamic impact process is explored following the T4 heat treatment process. This should provide guidance in the design and performance optimization of the 7055 aluminum alloy.

## METHODS

### Materials

Details on the composition of the material are given in Table I. The 7055 aluminum material was treated by T4. T4 includes solution treatment at 540°C for 2 h, followed by submersion in water, followed by natural aging for 336 h. The tensile strength, yield strength and elongation of the 7055 aluminum alloy after aging were 590 MPa, 550 MPa and 7.5%, respectively.

**Table I. Chemical composition of the 7055 aluminum alloy (wt%)**

Element	Zn	Mg	Cu	Zr	Fe	Si	Cr	Mn	Al
True value	7.76	1.94	2.35	0.12	0.061	0.055	0.005	0.008	Allowance
Nominal value	7.6 ~ 8.4	1.8 ~ 2.3	2.0 ~ 2.6	0.08 ~ 0.25	< 0.15	0.10	< 0.04	< 0.05	Allowance

## DYNAMIC IMPACT EXPERIMENT

The equipment for the dynamic impact experiment is shown in Fig. 1. The sample size was  $\varphi 8 \times 6$ -mm pieces of aluminum. The experiment was carried out at four temperatures: room temperature (approximately 20°C), 120°C, 220°C and 320°C. The projectiles were made of copper-clad steel, and their impact pressure was in the range of 0.25 MPa ~ 0.7 MPa

## FINITE ELEMENT MODEL

This study is intended to establish an accurate dynamic impact finite element (FE) model. Material attribute and material damage behavior modeling is a prerequisite for any dynamic impact simulation, and so we propose a theoretical model of large plastic deformation.<sup>4</sup> According to the findings of Liguishery, plastic deformation energy during the process of large plastic deformation can be described by the empirical formula shown in Eq. 1.

$$\begin{aligned} \varphi(\varepsilon_x, \sigma_x, r, d) &= \varphi_x(\varepsilon_x, d) + \varphi_e(\sigma_x, r) \\ &= \frac{1}{2}(1-d)\varepsilon_x : D : \varepsilon_x + \varphi_{\text{iso}}(r) \\ &\quad + \frac{1}{2} \sum_{k=1}^M \sigma_x \varepsilon_x^{m-1} : \sigma_x \end{aligned} \quad (1)$$

where  $\alpha_k$  is an internal kinematic variable,  $\gamma$  is the hardening parameter, and  $d$  is the damage variable. According to the variable principle for damage modeling, damage variable  $d$  can be written as Eq. 2:

$$\begin{aligned} d &= 1 - \left[ \left( \frac{\varepsilon}{\varepsilon_0} \right)^m + 1 \right] \exp \left( - \left( \frac{\varepsilon}{\varepsilon_0} \right)^m \right) \\ &\quad \times \left( 1 - \left( \frac{T - T_{\text{room}}}{T_{\text{melt}} - T_{\text{room}}} \right)^{m-r} \right) \end{aligned} \quad (2)$$

During dynamic impact, the temperature rise in the shear zone results in the formation of an obvious adiabatic shear zone, and the temperature rise model of such an adiabatic shear zone is very critical for determining the dynamic impact damage.<sup>5,6</sup> Hence, the adiabatic temperature rise model can be written as Eq. 3:

$$T = \frac{((\tau_{sw} - \tau_{sw0})V^\lambda - \Delta G_0^\zeta)}{k \ln \left( \frac{\dot{\varepsilon}}{\dot{\varepsilon}_0} \right)} \quad (3)$$

By introducing Eq. 3 into Eq. 2, we can establish a mathematical model of damage parameter  $d$  as shown in Eq. 4:



Fig. 1. Split Hopkinson press bar.

$$\begin{aligned} d &= 1 - \left[ \left( \frac{\varepsilon}{\varepsilon_0} \right)^m + 1 \right] \exp \left( - \left( \frac{\varepsilon}{\varepsilon_0} \right)^m \right) \\ &\quad \times \left( 1 - \left( \frac{\left( (\tau_{sw} - \tau_{sw0})V^\lambda - \Delta G_0^\zeta \right) - T_{\text{room}}}{k \ln \left( \frac{\dot{\varepsilon}}{\dot{\varepsilon}_0} \right)} \right)^{m-r} \right) \end{aligned} \quad (4)$$

Given that the strain during dynamic impact satisfies the superposition theorem and the level of internal strain directly decides the level of thermodynamic force,<sup>7</sup> the relationships between the superposition theorem and thermodynamic force are expressed by Eqs. 5–9:<sup>8,9</sup>

$$\varepsilon = \varepsilon_x + \varepsilon_e + \varepsilon_\tau \quad (5)$$

$$\varphi(\varepsilon_x) = \frac{m}{\alpha} \varepsilon_x^{m-1} \exp \left( - \frac{\varepsilon_x^m}{\alpha} \right) \left( \frac{\varepsilon_e}{\varepsilon_\tau} \right)^{m-r} \quad (6)$$

$$\sigma_x = E \varepsilon_x (1 - D) = E \varepsilon_x \exp \left( - \frac{\varepsilon_x^m}{\alpha} \right) \left( \frac{\varepsilon_e}{\varepsilon_\tau} \right)^{m-r} \quad (7)$$

$$X_k = \frac{\partial \varphi}{\partial \sigma_x} = \sigma_x \varepsilon_x^{m-1} \varepsilon_e^{k-r} \varepsilon_\tau^m \quad (8)$$

$$Y = - \frac{\partial \varphi}{\partial d} = \frac{1}{2} \varepsilon_x : D : \varepsilon_e : d : \varepsilon_\tau \quad (9)$$

where  $\sigma$  is a tensor factor,  $D$  is the plastic damage factor,  $R$  is the heat hardening factor,  $X$  is the inverse tensor parameter, and  $Y$  is the thermal damage force factor.

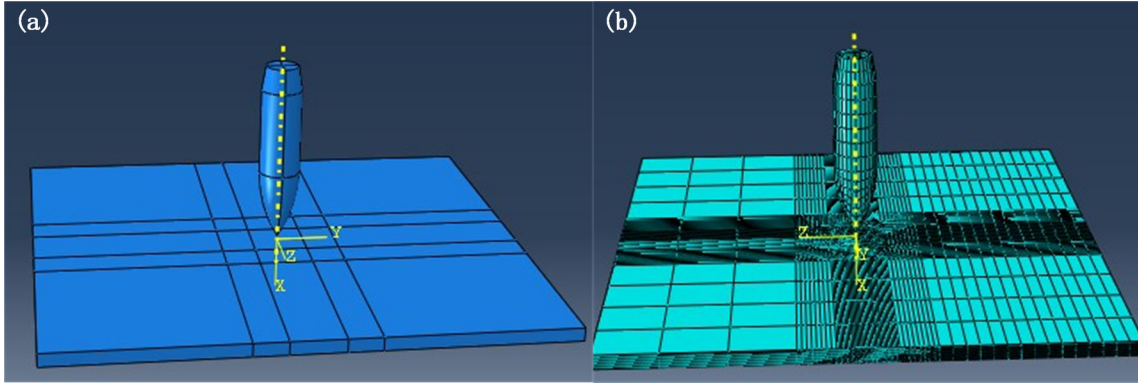


Fig. 2. Geometric model (a) and grid units (b).

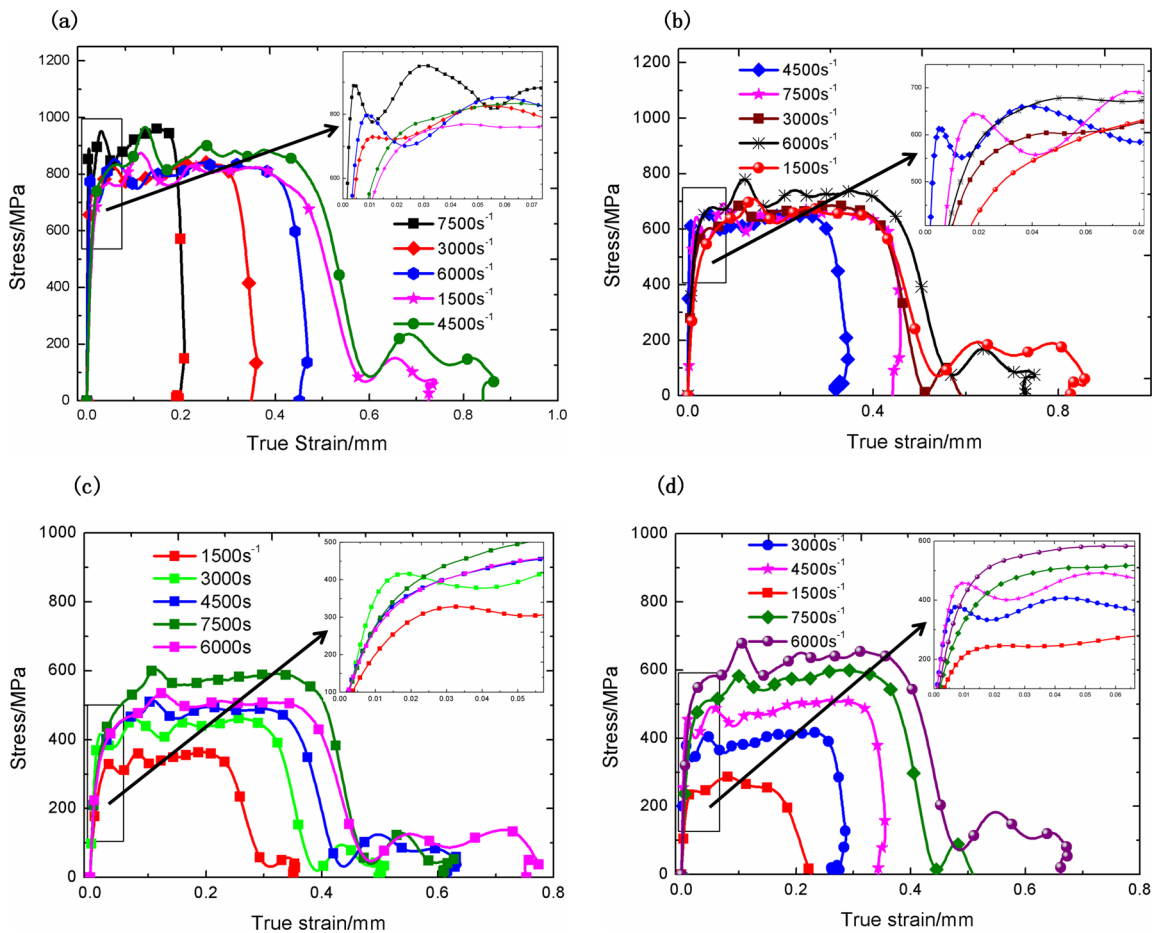


Fig. 3. Rheologic stresses at different temperatures and strain rates. (a) Rheologic stresses at 20°C; (b) rheologic stresses at 120°C; (c) rheologic stresses at 220°C; (d) rheologic stresses at 320°C.

Damage evolution follows a given rule—normally the complementary dissipated potential energy principle. Evolution equations are established based on this principle as shown in Eqs. 10–14:

$$E' = \frac{Gb^2 f(v)}{4\pi} \ln\left(\frac{\gamma}{\gamma_0}\right) \quad (10)$$

$$G = \frac{3\gamma_0 \varepsilon}{D \varepsilon_s} \left(\frac{\dot{\varepsilon}_e}{\dot{\varepsilon}_\tau}\right)^{m-r} \left(1 - \ln \frac{\gamma_0}{\gamma}\right) \quad (11)$$

$$\gamma = \frac{\gamma_0 \dot{\varepsilon}}{\alpha_k} \left(\frac{\dot{\varepsilon}_e}{\dot{\varepsilon}_\tau}\right)^{m-r} \left(1 - \ln \frac{Y}{\sigma}\right) \quad (12)$$



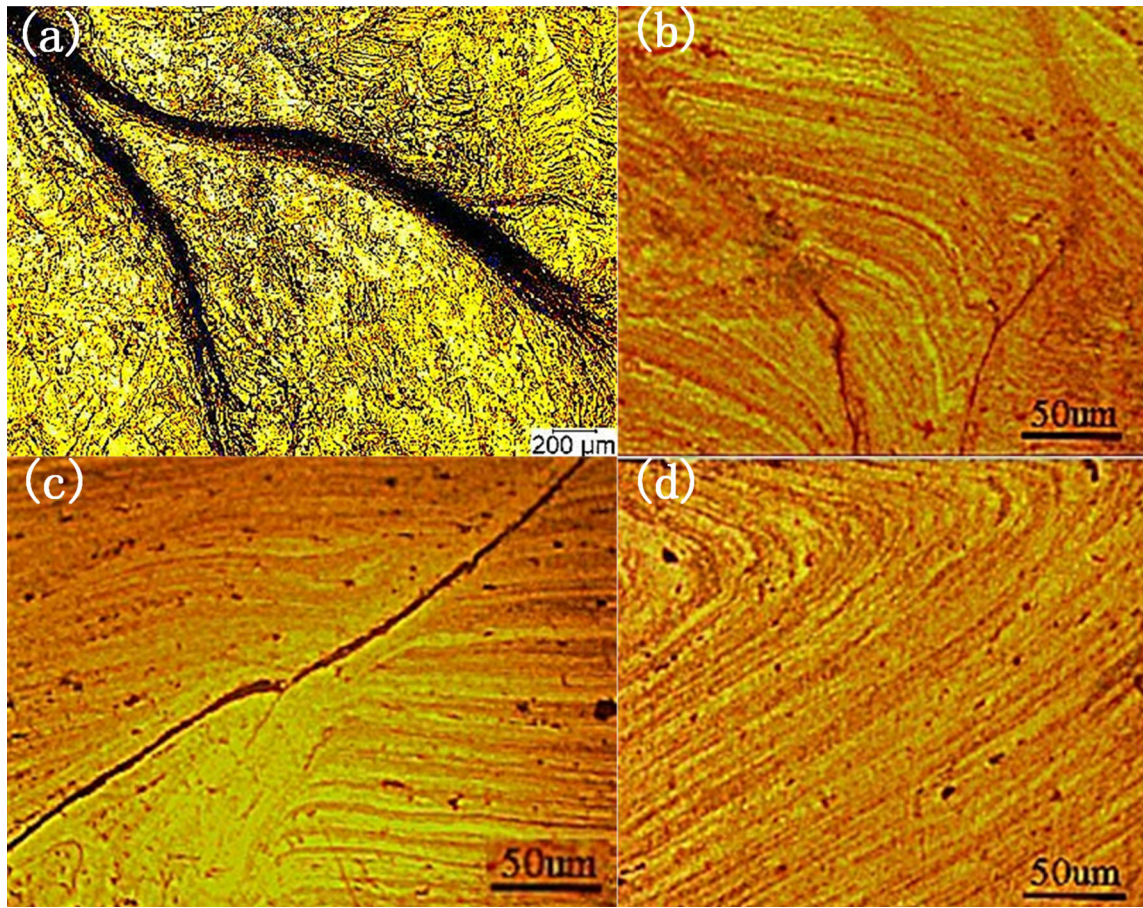


Fig. 4. Microstructure of adiabatic shear at different temperatures. (a) Microstructure of adiabatic shear under 20°C; (b) microstructure of adiabatic shear under 120°C; (c) microstructure of adiabatic shear under 220°C; (d) microstructure of adiabatic shear under 320°C.

$$\frac{1}{\sigma} \frac{d\sigma}{d\varepsilon} = \frac{X}{\varepsilon} (\dot{\varepsilon}_x + \dot{\varepsilon}_e + \dot{\varepsilon}_\tau) + \frac{Y}{\dot{\varepsilon}} (\dot{\varepsilon}_x + \dot{\varepsilon}_e + \dot{\varepsilon}_\tau) + \frac{1+X+Y}{F} \frac{dF}{d\varepsilon} - \frac{Y}{\rho} \frac{d\sigma}{d\varepsilon} \quad (13)$$

$$F = f - \frac{1}{2} \sum_{k=1}^M \frac{b}{\alpha_k} X : Y + F_d(Y, d) \quad (14)$$

where  $\gamma$  is the plastic multiplier,  $\varepsilon_s$  is the shear damage heat transfer factor, and  $F_d$  is the shear damage thermodynamic force of the material. A complete reverse Euler integral transformation of the evolution equations shown in Eqs. 10–14,<sup>10,11</sup> and subsequent simplification, yields models shown in Eqs. 15 and 16.

$$f_1(\gamma, \varepsilon_s) = \frac{\sqrt{3/2}E'}{(1-\gamma)^\delta} - \sigma = 0 \quad (15)$$

$$f_2(\gamma, \varepsilon_s) = \varepsilon_s - \varepsilon_{sn} - \delta \left( \frac{\varepsilon_e}{\varepsilon_\tau} \right) - \gamma Y = 0 \quad (16)$$

Considering the characteristics of the centrosymmetric model,<sup>12</sup> the structural element, mesh element and boundary condition model of dynamic

impact are established as shown in Fig. 2. The boundary condition of the target plate is that it is completely fixed.

## RESULTS AND DISCUSSION

### Rheologic Stress Relations

Figure 3 shows the rheologic stress relationship under different temperatures and impact pressures. The alloy behaves as expected under all temperature and impact conditions. Under all dynamic impact temperatures, after dynamic shock, there is an obvious positive correlation between the material's flow stress and strain rate.<sup>13</sup> When the temperature is > 220°C, the material displays a thermal softening effect.<sup>14,15</sup> Figure 4 also shows that under the same conditions, all the dynamic impact test specimens display an obvious adiabatic shear zone at 20°C, 120°C and 320°C, and the width of this adiabatic dynamic zone is strongly positively correlated with the dynamic impact temperature.

Figure 5 describes the stress–strain cloud of the 7055 aluminum alloy at different dynamic impact response times under different impact velocities when the dynamic impact temperature is 20°C. As the dynamic impact velocity increases, the dynamic

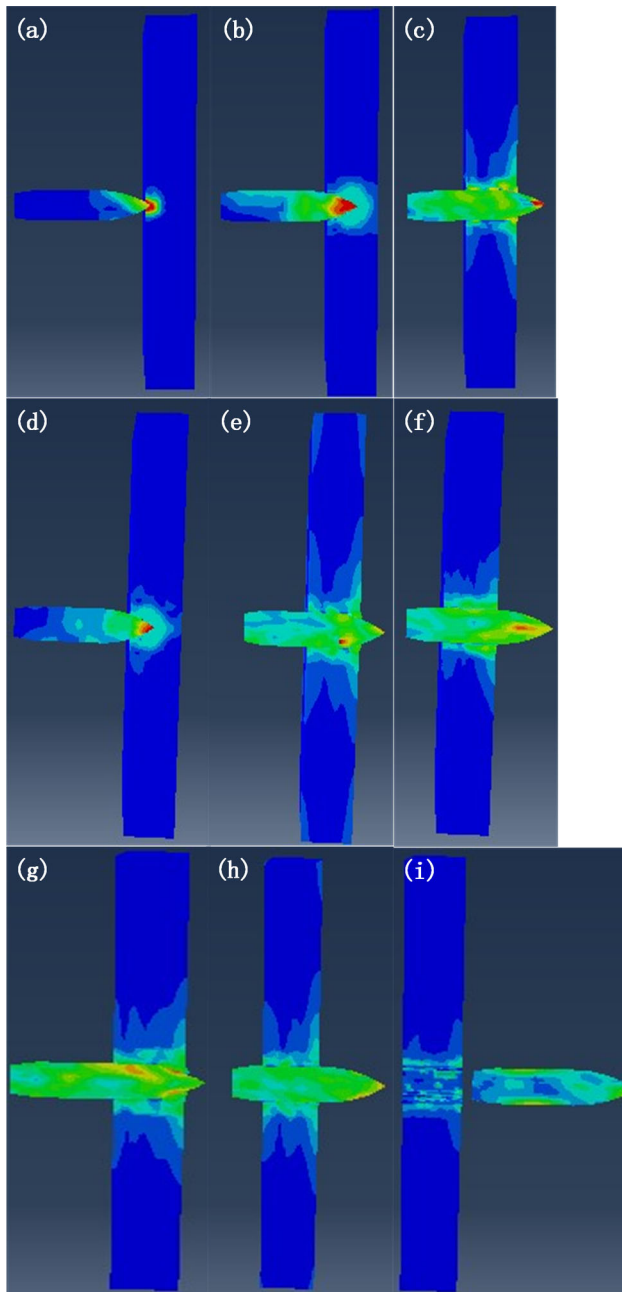


Fig. 5. Deformation cloud diagram of different impact speeds. (a) 10 m/s, 0.5 s; (b) 10 m/s, 1 s; (c) 10 m/s, 1.5 s; (d) 30 m/s, 0.5 s; (e) 30 m/s, 1 s; (f) 30 m/s, 1.5 s; (g) 50 m/s, 0.5 s; (h) 50 m/s, 1 s; (i) 50 m/s, 1.5 s.

impact response time needed for the bullet to penetrate the target decreases. When the projectile penetration velocity is 10 m/s, the dynamic response time for the bullet to penetrate the target is 1.5 s.

When the projectile penetration velocity is 30 m/s and 50 m/s, the dynamic response time required for the bullet to penetrate the target is 1 s in both cases. When the projectile penetration velocity is 50 m/s, the bullet has completely penetrated the target by the dynamic response time of 1.5 s. This is not the case for bullets traveling 30 m/s. The alloy displays obvious strain rate stiffening during dynamic impact at 20°C. As the bullet velocity increases, the dynamic impact strain rate also increases. Hence, as the yield strength increases, so does the heat produced from the bullet penetrating the target.<sup>16</sup> However, when the dynamic impact velocity is too high, most of the heat produced from the impact is converted, causing a transient regression in the material near the projectile trajectory.

Figure 6 describes the rheologic stress cloud of the 7055 aluminum alloy at different projectile penetration response times under high-temperature dynamic impact. Under constant dynamic impact response times at 220°C, the dynamic impact rheologic stress is the largest at approximately  $1.643 \times 10^9$ . The dynamic impact rheologic stress was smallest at 320°C. At 120°C, the dynamic impact rheologic stress is slightly lower than that at temperatures < 120°C, but far higher than that at 320°C—about 1.4 times as high. Under a constant dynamic impact temperature, the dynamic impact rheologic stress decreases with impact response time. As the dynamic impact ambient temperature increases, the 7055 aluminum alloy is softened to some extent.<sup>17</sup> As the strain rate increases, strain rate stiffening obviously prevails. When the dynamic impact temperature is 220°C, strain rate stiffening is coupled with thermal softening, and the material reaches its maximum yield strength, which is far higher than its yield strength under 120°C or 320°C. When the dynamic impact temperature is 320°C, heat conversion from the dynamic impact is coupled with strain rate stiffening, and the temperature of the alloy near the loading port becomes largely different from the aging stiffening temperature, causing a level of regression.<sup>18</sup>

Figure 7 describes the damage mode of the bullet hole at room temperature (20°C) and at 320°C. At 320°C, the stress damage area of the bullet opening is far larger than that under 20°C, but at 20°C, tearing damage appears at the bullet opening. By comparison with the stress-strain cloud of the damage on the back of the bullet opening, when the dynamic impact temperature is 20°C, an X-shaped tear appears at the bullet opening. No visible crack is observed at the bullet opening at 320°C.



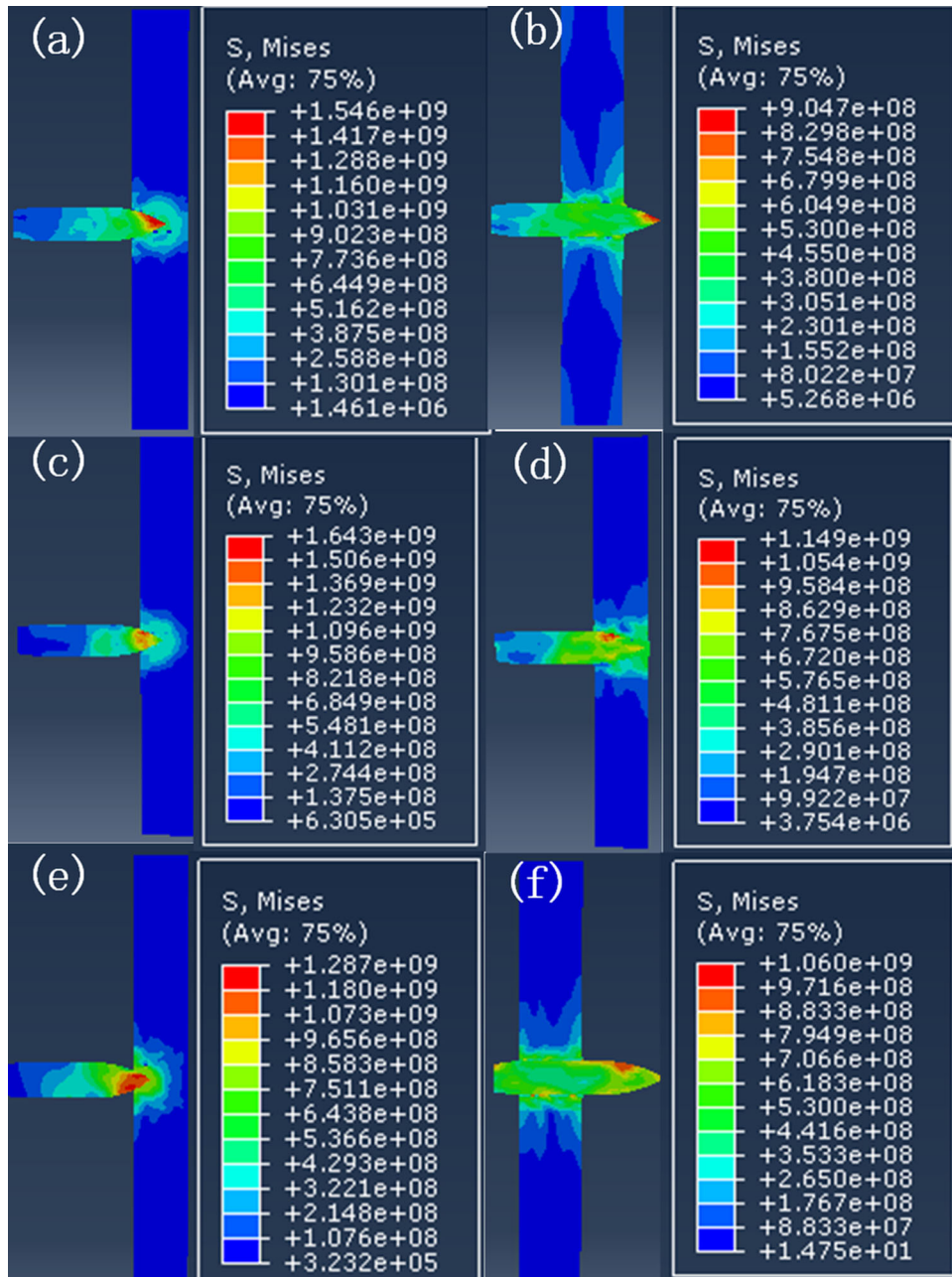


Fig. 6. Simulation results of different temperatures at the same speed. (a) Stress nephogram of 0.5 s under 120°C; (b) stress nephogram of 1.5 s under 120°C; (c) stress nephogram of 0.5 s under 220°C; (d) stress nephogram of 1.5 s under 220°C; (e) stress nephogram of 0.5 s under 320°C; (f) stress nephogram of 1.5 s under 320°C.

### NANOSCALE PRECIPITATE

Figure 8 describes the nano-scale precipitated phase of the 7055 aluminum alloy after dynamic impact under different dynamic impact conditions. When the strain rate is  $2000 \text{ s}^{-1}$ , as the dynamic impact temperature rises, the  $\theta'$  precipitates

gradually become less dense and larger in size. At 320°C, the  $\theta'$  precipitates become about 2.5 times as thick as they were at 120°C. When the strain rate is  $4000 \text{ s}^{-1}$ , the precipitates after dynamic impact are mostly composed of both  $\theta'$  precipitates and  $\theta$  particles.<sup>19</sup> As the dynamic impact temperature

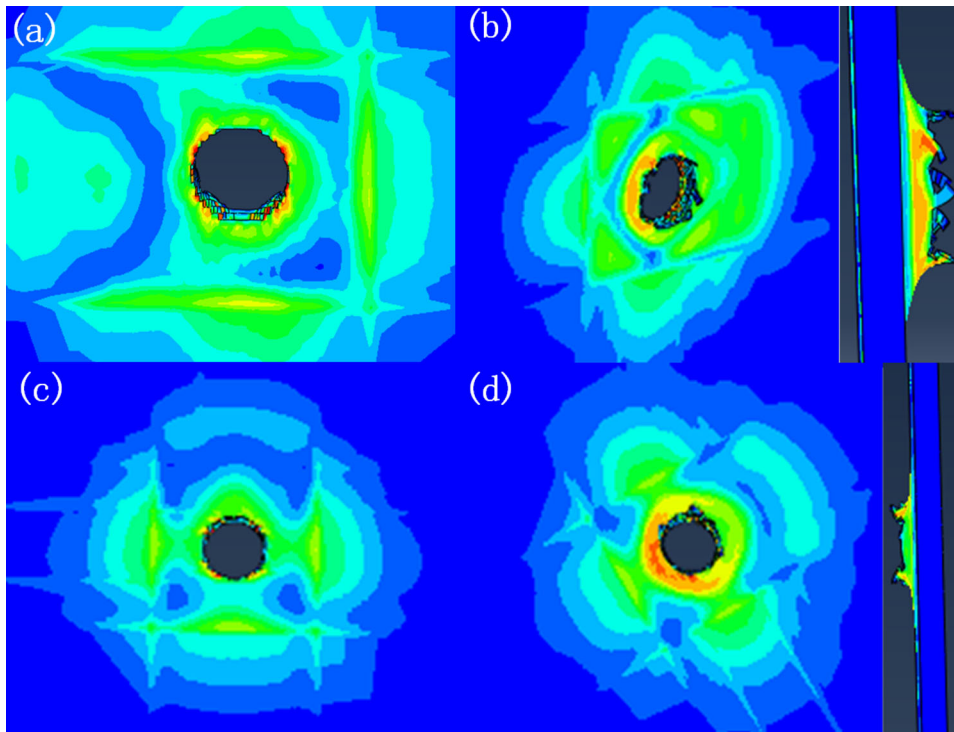


Fig. 7. Damage mode of the bullet hole at room temperature (20°C) and high temperature (320°C). (a) Front damages of the cutout at 20°C; (b) back damages of the cutout at 20°C; (c) front damages of the cutout at 320°C; (d) back damages of the cutout at 320°C.

rises, the density of the  $\theta$  particles gradually increases to the point where they are denser than the  $\theta'$  precipitates at 320°C. When the strain rate is  $6000 \text{ s}^{-1}$ , the precipitates in the test specimens at 220°C and 320°C were all steady-phase  $\theta$  particles. At 320°C, the precipitates are all approximately twice as large as they were at 220°C. At 120°C, they were composed of both  $\theta'$  precipitates and  $\theta'$  particles, though the  $\theta$  particles were smaller than they were under 220°C. When the dynamic impact temperature is  $< 120^\circ\text{C}$ , the large plastic deformation can be regarded as a cold rolling process. A lot of the kinetic energy of the alloy is converted into thermal energy and accumulates within the material for a short time when the strain rate is  $> 6000 \text{ s}^{-1}$ . High-velocity impacts will expose the material to great pressure and induce in it an adiabatic temperature rise, speeding up the dispersion of the dislocated atoms within the material.<sup>20</sup> It follows that the precipitates will transform into  $\theta'$  steady particles. As the dynamic impact temperature rises beyond 220°C, incomplete dynamic recovery, accompanied by dynamic recrystallization, will take place inside the alloy. However, as the dynamic impact is too short to achieve complete dynamic recovery, there are still many dislocations.<sup>21,22</sup>

## CONCLUSION

- (1) Under the same conditions, all the dynamic impact test specimens display an obvious adiabatic shear zone at 20°C, 120°C and 320°C, and the width of this adiabatic dynamic zone is obviously positively correlated to the dynamic impact temperature; the test specimens do not show any obvious adiabatic shear zone except a level of the rheologic zone  $> 320^\circ\text{C}$ .
- (2) When the dynamic impact temperature is 20°C, an X-shaped tear appears at the bullet opening; when the dynamic impact temperature is 320°C, no visible crack is observed at the bullet opening.
- (3) When the strain rate is  $6000 \text{ s}^{-1}$ , the precipitates in the test specimens treated under the dynamic impact temperatures of 220°C and 320°C are all steady-phase  $\theta$  particles, and the precipitates treated under the dynamic impact temperature of 320°C are all about twice as large as they were under 220°C, but those treated under the dynamic impact tempera-

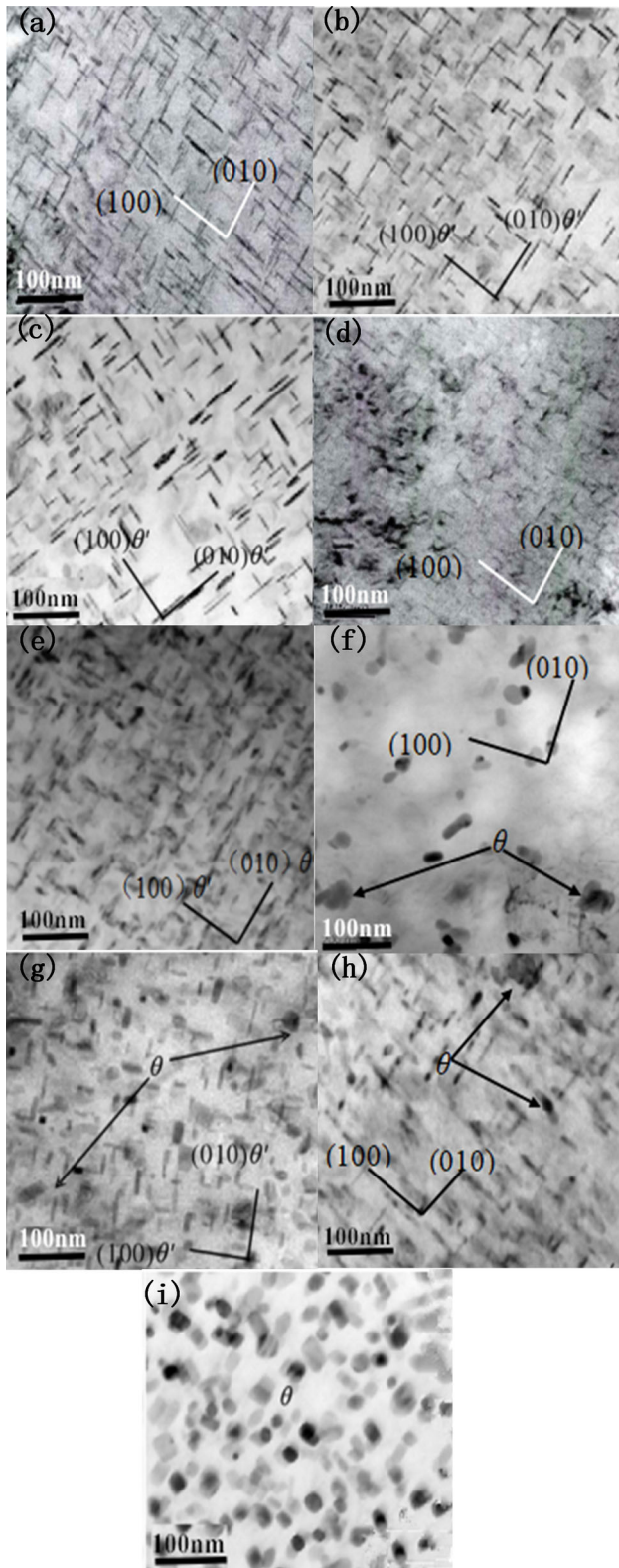


Fig. 8. Effects of strain rate on TEM BF images along  $[001]_{Al}$ . (a)  $120^{\circ}\text{C}$ ,  $2000\text{ s}^{-1}$ ; (b)  $220^{\circ}\text{C}$ ,  $2000\text{ s}^{-1}$ ; (c)  $320^{\circ}\text{C}$ ,  $2000\text{ s}^{-1}$ ; (d)  $120^{\circ}\text{C}$ ,  $4000\text{ s}^{-1}$ ; (e)  $220^{\circ}\text{C}$ ,  $4000\text{ s}^{-1}$ ; (f)  $320^{\circ}\text{C}$ ,  $4000\text{ s}^{-1}$ ; (g)  $120^{\circ}\text{C}$ ,  $6000\text{ s}^{-1}$ ; (h)  $220^{\circ}\text{C}$ ,  $6000\text{ s}^{-1}$ ; (i)  $320^{\circ}\text{C}$ ,  $6000\text{ s}^{-1}$ .

ture of  $120^{\circ}\text{C}$  are still composed of both  $\theta'$  precipitates and  $\theta$  particles, though the  $\theta$  particles are smaller than they were under  $220^{\circ}\text{C}$ .

### ACKNOWLEDGEMENTS

This study was supported by the National Natural Science Foundation of the China Youth Fund and the First Project (No. 51705270), National Natural Science Foundation of China (51575289), Shandong Natural Science Foundation Doctoral Fund (No. ZR2016EEP03) and A Project of the Shandong Province Higher Educational Science and Technology Program (No. J17KA0031).

### REFERENCES

1. Y. Yang, X. Li, C. Xu, L. Zhang, Q. Zhang, and X. Tong, *J. Mater. Eng. Perform.* 21, 197 (2012).
2. Y. Yang, Z. Zhang, X. Li, Q. Wang, and Y. Zhang, *Mater. Des.* 51, 592 (2013).
3. M. Tajally, Z. Huda, and H.H. Masjuki, *Int. J. Impact Eng.* 37, 425 (2010).
4. Y. Cao, A. Feng, and G. Hua, *J. Appl. Phys.* 116, 775 (2014).
5. P. Zhang and Y. Wang, *Vacuum* 152, 150 (2018).
6. A.S. Mahdi, M.S. Mustapa, A.L.M. Tobi, and I. Zaman, *Mater. Sci. Forum* 887, 74 (2017).
7. K. Labisz, T. Tański, D. Janicki, W. Borek, K. Lukaszewicz, and L. Dobrzański, *Arch. Metall. Mater.* 61, 741 (2016).
8. K.K. Babu, K. Panneerselvam, P. Sathiyaa, A.N. Haq, S. Sundarrajan, P. Mastanaiah, and C.V. Srinivasa Murthy, *Mater. Today Proc.* 4, 285 (2017).
9. P. Zhang and Y. Wang, *Vacuum* 151, 243 (2018).
10. J. Konieczny, K. Labisz, M. Polokrubiniec, and A. Włodarczykfligier, *Arch. Metall. Mater.* 61, 1337 (2016).
11. M. Qi, C. Luo, H. He, Y. Wang, D. Fan, and S. Yan, *J. Appl. Phys.* 111, 043506 (2012).
12. J.Z. Lu, K.Y. Luo, Y.K. Zhang, J.Z. Zhou, X.G. Cui, L. Zhang, and J.W. Zhong, *Mater. Sci. Eng. A-Struct.* 528, 730 (2010).
13. L. Oger, E. Andrieu, G. Odemer, L. Peguet, and C. Blanc, *Mater. Sci. Forum* 877, 1107 (2017).
14. Z. Zhan, W. Hu, Q. Meng, and S. Shi, *Int. J. Damage Mech.* 25, 342 (2016).
15. C. Su, J. Zhou, X. Meng, and S. Huang, *Materials* 9, 799 (2016).
16. B. Çevik, Y. Özçatalbaş, and B. Gülenç, *Prakt. Metallogr-PR M* 53, 6 (2016).
17. R. Singh, R.K. Khatirkar, R.N. Chouhan, and S.G. Sapate, *Trans. Indian Inst. Met.* 69, 1 (2016).
18. M. Sharma, G.K. Gupta, R. Dasgupta, M. Kumar, and P. Kumar, *Trans. Indian Inst. Met* 36, 1 (2018).
19. J.M. Liang, C. Kong, M.Z. Quadir, Y.F. Zheng, X. Yao, P. Munroe, and D.L. Zhang, *Mater. Sci. Eng. A-Struct.* 658, 192 (2016).
20. A. Kumar, A. Patnaik, and I.K. Bhat, *Powder Metall.* 125, 1 (2017).
21. D. Bolibruchová, L. Richtárech, S.M. Dobosz, and K. Majorgabryś, *Arch. Metall. Mater.* 62, 339 (2017).
22. W.S. Lee, W.C. Sue, C.F. Lin, and C.J. Wu, *J. Mater. Process. Tech.* 100, 116 (2000).

**Publisher's Note** Springer Nature remains neutral with regard to jurisdictional claims in published maps and institutional affiliations.